# Determination of Johnson–Cook parameters and evaluation of Charpy impact test performance for 1.2709 steel produced via L-PBF

**Balázs Lőrincz**
PhD Student
Széchenyi István University
Department of Materials Engineering and Machine Design
Hungary

**István Hatos**
Associate Professor
Széchenyi István University
Department of Materials Engineering and Machine Design
Hungary

*Laser powder bed fusion (L-PBF) enables the creation of advanced metal parts that are difficult to manufacture conventionally. In this study, the model parameters of the Johnson–Cook (JC) constitutive relation and the damage parameters of the JC failure model for 1.2709 steel produced via L-PBF were determined. Constitutive parameters were identified from quasi-static uniaxial tensile tests conducted on smooth specimens. In contrast, stress triaxiality-dependent damage parameters were determined using tensile tests on notched round bar specimens in combination with FEM simulations. The load–displacement curves showed good agreement with the experimentally obtained data. The strain–rate–dependent failure model parameter was determined by correlating Charpy impact test results with numerical simulations. Reasonable agreement between the simulation and experimental results was achieved. The results demonstrate that the proposed experimental–numerical framework provides a reliable basis for modelling both the quasi-static and impact fracture behaviour of L-PBF-fabricated 1.2709 steel.*

***Keywords:****additive manufacturing, L-PBF, 1.2709 steel, Charpy impact test, Johnson-Cook model*

## 1. INTRODUCTION

Laser powder bed fusion (L-PBF) is one of the most commonly used metal additive manufacturing (AM) technologies. L-PBF uses a focused laser beam to melt powdered metallic particles, forming highly dense com–ponents layer by layer according to a 3D model. Mara–ging steels are easy to print, and 1.2709 (18Ni300) is the most widely used maraging steel in L-PBF; it is exten–sively employed in tooling and aerospace applications [1-3]. However, the multiphysics nature of the L-PBF process often leads to defect formation, which can ne–gatively affect the mechanical properties of the fabri–cated parts. Despite these challenges, L-PBF enables the printing of geometrically complex components with a high degree of design freedom [4,5].

The finite element method (FEM) is a numerical approach used to analyse and predict the mechanical behaviour of complex structures. Studies on the FEM simulation of parts obtained through metal AM have attracted increasing attention in recent years. Among various constitutive models, the Johnson–Cook (JC) model is frequently employed in FEM simulations due to its simple form and the relative ease of determining its parameters. It is widely used to study impact loading or similar problems involving metals.Numerous studies have investigated the determination of JC parameters for 1.2709 AM materials produced by L-PBF. Dehgahi et al. [6] characterised the dynamic response of as-built 1.2709 specimens using a Split Hopkinson Pressure Bar apparatus. Kolomy et al. [7] investigated the high-strain-rate behaviour of 1.2709 steel via the Taylor anvil test. The acquired data were incorporated into the JC constitutive equation for numerical simulation, demon–strating satisfactory agreement with the experimental results. Liang et al. [8] studied the JC constitutive model for specimens printed in different build directions and reported close correspondence between simulated and measured strain rate–time curves. Eisseler et al. [9] applied a simplified inverse method to determine the build-direction-dependent parameters of a modified JC model for cutting simulations. Additionally, Edwards-Mowforth et al. [10] analysed the ballistic impact response of 1.2709 steel. Cylindrical specimens for uniaxial tensile tests and target plates for ballistic impact tests were printed for the experiments, and the experimentally and numerically determined ballistic limit velocities agreed to within 10%.

In contrast to tensile properties, the impact pro–perties of AM metals—typically determined through the Charpy impact test—are rarely documented in the sci–entific literature. Sagar et al. [11] investigated the Charpy impact properties of printed 15-5 stainless steel through a combined experimental and FEM study, de–veloping a JC model with damage parameters to simulate the impact tests.

Despite these advances, the existing literature lacks comprehensive quasi-static and dynamic experimental characterisation, as well as validated virtual material modelling, of additively manufactured maraging steel. To address these gaps, the present study develops and

Received: December2025, Accepted: February 2026
Correspondence to: Dr Istvan Hatos
Széchenyi István University,
Egyetem tér 1, 9026 Győr, Hungary
E-mail: hatos@sze.hu
**doi: 10.5937/fme2602226L**

validates a material model suitable for reliable appli–cation in industrial practice.

To the best of the authors' knowledge, the room-temperature impact behaviour of 1.2709 components produced by L-PBF has not been numerically simulated previously. Therefore, in this study, the mechanical response of an L-PBF 1.2709 alloy has been investi–gated through comprehensive experiments. The JC con–stitutive parameters were determined from a quasi-static uniaxial tensile test of a smooth bar specimen. In contrast, the damage parameters associated with stress triaxiality were obtained from tensile tests on notched bar specimens. Thereafter, the Charpy impact test—representative of moderately high strain-rate loading—was simulated. Based on the experimental results, the strain rate-related damage parameter was determined, and the reliability of the FEM predictions was assessed.

There is growing use of 3D-printed steel structures in military (e.g., armour) and civilian applications (e.g., space technology, motorsport, and machining tools). The Johnson–Cook parameters defined in this publica–tion provide an accurate description of material beha–viour, allowing design engineers to determine material thicknesses and appropriate geometries necessary for safe operation and high performance.

## 2. EXPERIMENTAL METHODS

### 2.1 Sample fabrication

All specimens in this study were manufactured using an EOSINT M270 system equipped with a 200 W Yb-fibre laser (wavelength: 1070 nm, focus diameter: 100 μm) operated under a protective nitrogen gas atmosphere. Maraging steel 1.2709 powder supplied by M4p Mate–rials Solutions GmbH served as the raw material. This alloy is internationally designated as 18Ni (300-grade) maraging steel or X3NiCoMoTi 18-9-5. Before proces–sing, the powder was sieved to ensure only particles with a diameter of 80 μm or less were used.

The applied process parameters were as follows: a laser power of 150 W, scanning speed of 600 mm/s, hatch distance of 0.1 mm, and layer thickness of 20 μm. The build platform was maintained at 40 °C. A stripe-hatching strategy was employed, with a 67° scanning rotation between consecutive layers and omitting con–tour scans. These parameters were selected to ensure the production of parts with near-full density, as re–ported in a previous study [12].

### 2.2 Test geometries

Charpy impact specimens and cylindrical bars with dimensions of Ø10 mm × 70 mm for tensile testing were printed in the vertical build direction. The gauge regions of the unnotched Ø6 mm tensile specimen and three different notched tensile variants were subsequently machined to their final geometry using a computer numerical control (CNC) lathe (Figure 1). The dimen–sional schematic of the notched bar specimens is pre–sented in Figure 2, with notch radii R of 0.8 mm, 2.25 mm, and 4.85 mm.

**Figure 1. Machined tensile test specimens**

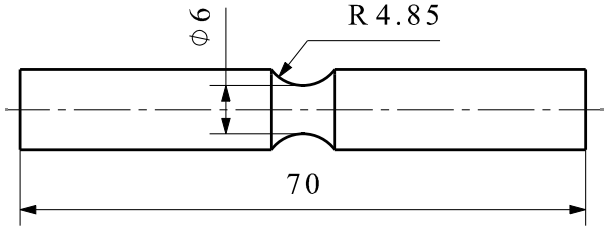


**Figure 2. Notched tensile specimen with notch radii R of 4.85 mm**

The Charpy impact specimens featured a square cross-section of 10 mm × 10 mm, a total length of 55 mm, and a 2 mm deep notch with a root radius of 0.25 mm positioned at mid-length. All mechanical tests were carried out on specimens in the as-built condition; no stress-relief or ageing heat treatments were applied.

## 3. DETERMINATION OF JC MODEL PARAMETERS

### 3.1 Johnson–Cook constitutive model

In 1983, Johnson and Cook proposed a material model that describes the coupled influence of strain, strain rate, and temperature on the flow stress of materials. In this formulation, the first bracket represents the strain har–dening dependence, the second bracket represents the strain rate dependence, and the third bracket describes the weakening effect of temperature [13,14]:

$$\sigma = \left(A + B\varepsilon^{n}\right)\left(1 + C\ln\frac{\dot{\varepsilon}}{\dot{\varepsilon}_0}\right)\left[1 - \left(\frac{T\text{-}T_{room}}{T_{melt}\text{-}T_{room}}\right)\right] \quad (1)$$

In this equation, $A$, $B$, $n$, $C$, and $m$ denote material-specific constitutive parameters. Specifically, $A$ repre–sents the initial yield strength, $B$ and $n$ correspond to the strain-hardening modulus and strain-hardening (work-hardening) exponent, $C$ is the strain-rate hardening parameter, and $m$ is the thermal softening parameter. $\sigma$ and $\varepsilon$ are the equivalent flow stress and plastic strain, respectively, while $\dot{\varepsilon}/\dot{\varepsilon}_0$ denotes the ratio of the current strain rate to the reference strain rate. The variables $T$, $T_{room}$, and $T_{melt}$ represent the current working tempe–rature, room temperature, and melting temperature of the material, respectively.

### 3.2 Determination of constant "*A*, *B*, *n*"

Quasi-static tensile tests were carried out using an Instron 5582 testing machine equipped with a 100 kN load cell. The tests were conducted at room temperature (~20 °C) and under a constant strain rate.


**Figure 3. Experimental setup for tensile test**

Under these testing conditions—at room temperature and a reference strain rate—the second and third terms of (1) become unity, allowing the JC model to be simplified to:

$$\sigma = A + B\varepsilon^{n}. \tag{2}$$

Tensile tests produced load-versus-deformation plots, which were converted to stress-versus-strain graphs. The tensile test results from the smooth (unnotched) tensile specimen are presented in Figure 4, showing both the engineering stress–strain and true stress–strain curves up to the onset of necking. The key tensile properties—such as yield stress, ultimate tensile stress, and Young's modulus—were extracted from the stress and strain graphs. Parameter $A$ was extracted directly from the initial yield point of the uniaxial tensile test, yielding an initial flow stress of $\sigma$ = 1180 MPa; that is, $A$ = 1180 MPa.

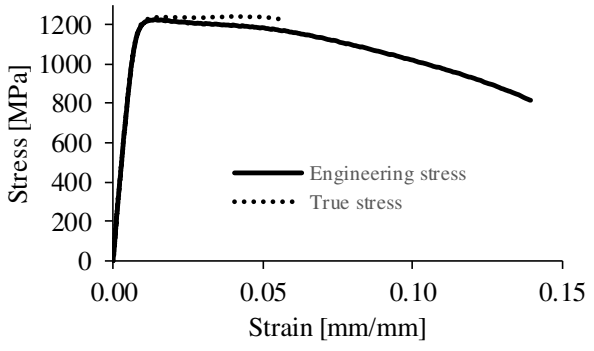


**Figure 4. Stress–strain curve from the quasi-static tensile test**

To determine $B$ and $n$, (2) was rearranged, and the natural logarithm was applied to both sides, producing a linear relationship as expressed in (3):

$$\ln(\sigma - A) = n\ln\varepsilon + \ln B. \tag{3}$$

A linear regression was then performed on the trans–formed data, and the slope and intercept of the fitted line yielded the strain-hardening modulus and strain-hardening exponent. From this fitting, $B$ and $n$ were determined to be 130 MPa and 0.1, respectively.

### 3.3 Johnson–Cook failure model

The damage criterion for ductile materials is based on the accumulation of plastic strain. The scalar damage parameter $D$ is defined as:

$$D = \sum \frac{\Delta\varepsilon}{\varepsilon_f} \tag{4}$$

where $\Delta\varepsilon$ denotes the increment of equivalent plastic strain and $\varepsilon_f$ is the equivalent strain to fracture. The damage parameter varies between 0 and 1, and damage initiation is assumed to occur when $D$ reaches 1 [15,16].

The Johnson–Cook fracture criterion describes the dependence of the fracture strain ($\varepsilon_f$) on stress tria–xiality, temperature, and strain rate. This model is par–ticularly well-suited for characterizing failure under high-strain-rate deformation, such as dynamic mono–tonic impact loading. It assumes that damage accumu–lates within the material during plastic deformation, which accelerates immediately when the damage reac–hes a critical value [16–19]. The failure model is expressed as:

$$\varepsilon_f = \left[D_1 + D_2 e^{D_3\eta}\right]\left(1 + D_4 \ln\frac{\varepsilon}{\varepsilon_0}\right)\left[1 + D_5\left(\frac{T - T_{room}}{T_{melt} - T_{room}}\right)\right] \tag{5}$$

In this expression, $D_1$–$D_5$ are material damage para–meters: $D_1$–$D_3$ are related to stress triaxiality, $D_4$ characterises strain rate sensitivity, and $D_5$ accounts for thermal effects. The variable $\eta$ represents the stress triaxiality.

The JC fracture model assumes that failure is initi–ated by the coalescence of voids located at the speci–men's centre. The determination of the JC failure para–meters, as defined in (5), requires knowledge of the stress triaxiality at the centre of the specimen. Stress triaxiality is defined as the ratio of the hydrostatic stress to the equivalent von Mises stress. This relationship is commonly investigated experimentally by performing tensile tests on round bars with various notch radii. For notched cylindrical specimens, the triaxiality factor can be estimated analytically from the notched geometry using the expression given in [16,20]:

$$\eta = \frac{1}{3} + \ln\left(1 + \frac{a}{2R}\right) \tag{6}$$

where $a$ is the radius of the necking cross-section, and $R$ is the radius of the notch root. This analytical formulation enables the estimation of the stress tria–xiality in the initial phase of tensile loading (Table 1).

**Table 1. Theoretical stress-triaxiality values**

| Notch radius [mm] | Stress triaxiality |
|---|---|
| ∞ | 0.33 |
| 4.85 | 0.60 |
| 2.25 | 0.84 |
| 0.8 | 1.39 |

However, analytical calculations inherently neglect both the spatial variation in stress triaxiality across the cross-section and the geometrical evolution that occurs during tensile deformation. Since stress triaxiality cannot be measured directly in experiments, it must be evaluated using FEM simulations. Figure 5 illustrates the stress triaxiality distributions along the longitudinal cross-sections of the tensile specimens at the fracture displacement, as determined by FEM. The stress triaxiality values differ substantially between the specimen centre and the lateral regions. Because the triaxiality is highest at the centre, this location is identified as the dominant site for damage initiation.

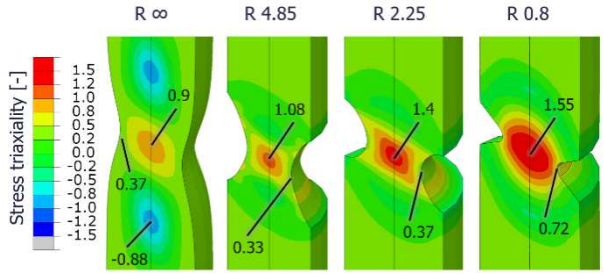


**Figure 5. Distribution of stress triaxiality from FEM analysis**

The numerical results demonstrate that the stress triaxiality values obtained from FEM deviate significantly from the analytical predictions. Consequently, analytical estimates of the JC damage initiation parameters are not sufficiently accurate, and numerical evaluation is required.

### 3.4 Determination of damage parameters $D_1$, $D_2$, and $D_3$

The tensile tests were completed under displacement control using a loading rate of 0.15 mm/s and at room temperature. Under these conditions, the effects of strain rate and temperature can be neglected, and the JC failure model reduces to the following simple form:

$$\varepsilon_f = D_1 + D_2 \exp(D_3 \eta). \quad (7)$$

In this representation, the relationship between fracture strain and stress triaxiality is exponential. The parameters $D_1$, $D_2$, and $D_3$ can be determined by establishing relationships between fracture strain and stress triaxiality across various stress states.

To determine these damage initiation parameters, quasi-static FEM simulations were performed using the ABAQUS/Standard solver on smooth and notched round bar specimens with notch radii $R$ of 0.8 mm, 2.25 mm, and 4.85 mm under uniaxial tensile loading.

Initial simulations showed no significant differences between the 3D and axisymmetric models; therefore, to reduce simulation time while enabling finer mesh refinement, only the axisymmetric model using the CAX element type was employed for subsequent analyses. To ensure numerical accuracy, elements with reduced integration were omitted. Instead, only fully integrated CAX4 (four-node bilinear axisymmetric quadrilateral) and CAX3 (three-node axisymmetric) elements were used, with hourglass control activated. A prescribed axial displacement was applied to one end of the specimen, whereas the opposite end—representing the grip region in the tensile experiment—was fully constrained (Figure 6). Consistency between the numerical simulation and the experimental setup was maintained by imposing the same displacement loading and extracting the reaction force at the designated control node.


**Figure 6. FEM model of quasi-static tension**

The damage parameters $D_1$, $D_2$, and $D_3$ were determined through an iterative calibration procedure, in which the onset of damage predicted by the finite element simulations was matched to the experimentally observed fracture strain for each specimen geometry. After multiple iterations, the parameter set $D_1 = 0.0688$, $D_2 = 6.566$, and $D_3 = -3.057$ was identified as providing an accurate representation of the experimentally measured initiation of failure. The resulting force–displacement responses obtained from the FEM simulations exhibit excellent agreement with the corresponding experimental curves for all investigated cases, as illustrated in Figure 7. Finally, the JC damage parameter shown in Figure 8 is obtained. A value of 1 indicates that the plastic strain has reached the stress triaxiality-dependent fracture strain limit. The value of this variable provides a clear picture of the material's reserve and the point at which failure occurs.

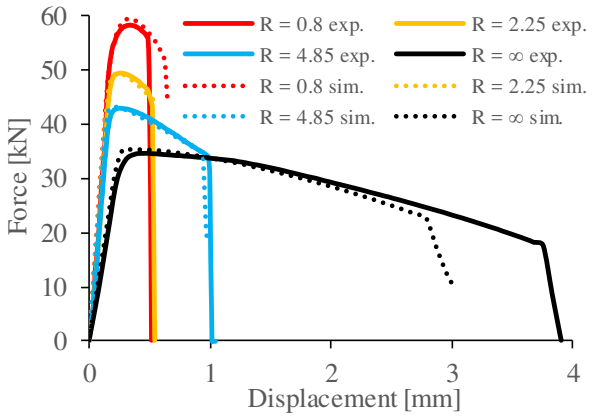


**Figure 7. Tensile force–displacement curves from simulation and experiment**

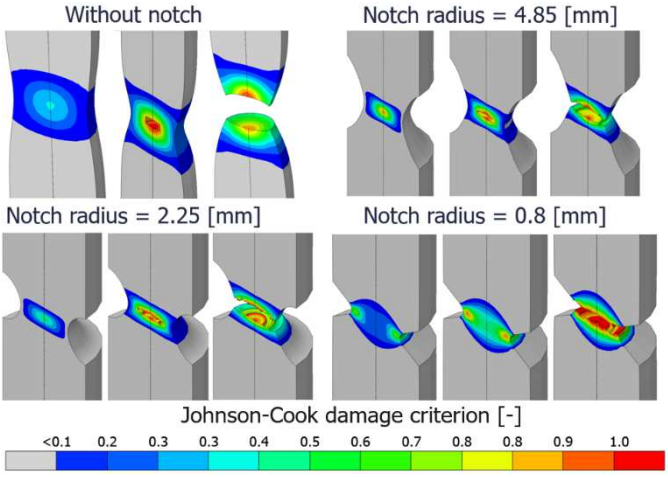


**Figure 8. Virtual tensile test results**

As summarised in Table 1, stress triaxiality increases as the notch radius decreases. The tensile force–disp–

lacement curves indicate that the fracture displacement decreases with increasing stress triaxiality, which corres–ponds to a reduction in notch radius. To further under–stand the significant differences in fracture strains caused by stress triaxiality, the 3D fracture surface morphology after tensile testing was characterised using a 3D optical scanner. The fracture surfaces of the tensile specimens were digitised using a GOM ATOS digital optical sys–tem. Figure 9 presents the final fracture surfaces of the tested specimens. The fracture morphologies of all four 1.2709 steel samples exhibited ductile fracture charac–teristics, including necking and a cup-and-cone shape. Furthermore, the fracture surfaces of all specimens were clearly divided into two distinct regions: a central pure cracking region (highlighted in red) and an outer shear lip region (highlighted in orange).

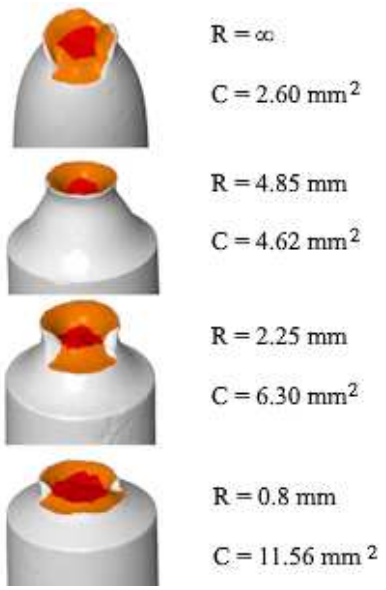


**Figure 9. Fracture surfaces of tensile test specimens, showing the measured cracking surface areas**

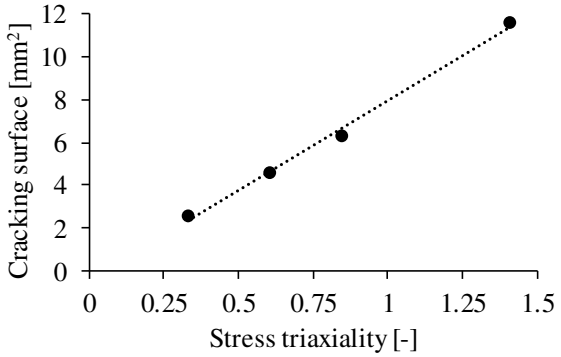


**Figure 10. Plot of stress triaxiality vs. cracking fracture surface**

To quantify the fracture surface characteristics, the scanned surface meshes were analysed using GOM Inspect and MaterialiseMagics software. The surface areas of the cracking regions (denoted as $C$) were deter–mined. The results demonstrate that the cracking surface area generally increases with increasing stress triaxiality (i.e., decreasing notch radius). This trend can be attri–buted to the enhanced hydrostatic tensile stress under higher stress triaxiality, which facilitates microvoid growth and coalescence. Figure 10 presents the relati–onship between stress triaxiality and the cracking sur–face area. A clear linear correlation is observed between stress triaxiality and the extent of the cracking fracture surface.

### 3.5 Determination of damage parameter $D_4$

The strain-rate-dependent failure model parameter $D_4$ was determined by correlating Charpy impact test re–sults with numerical simulations. Charpy tests were per–formed using a pendulum-type impact testing machine with a nominal energy of 300 J, following the ASTM E23 standard [21]. A striker with a 2 mm tip radius was employed, and all tests were performed at room tem–perature. During impact, the released striker followed a circular trajectory and delivered kinetic energy to the specimen at mid-span. In these experiments, the striker had a mass of 19.147 kg and a speed of 5.59 m/s. Pre–vious work reported a room-temperature Charpy impact energy of 119 J for L-PBF maraging steel printed with the same parameters [12].

The numerical simulation of the Charpy impact test was conducted as follows. The striker was modelled as a rigid body, whereas the specimen was assumed to be homogeneous and deformable. The specimen was discretised using 3D first-order hexahedral elements with reduced integration (C3D8R). A locally refined mesh was generated in the notch region, while a coarser mesh was used in the remaining areas of the specimen to reduce computational cost.

The impact load was assigned to the striker with an initial velocity of 5.59 m/s. The striker had a kinetic energy of 300 J, consistent with the operating conditions of the experimental apparatus. Contact between the stri–ker and the specimen was defined using a kinematic me–chanical constraint with frictional behaviour, assuming a friction coefficient of 0.12—a commonly adop–ted value for steel–steel interactions in engineering applications.

The transient dynamic response was simulated over a duration of 0.002 s following impact, within which fracture initiation and propagation occurred for all spe–cimens. The analysis was performed using the Abaqus/Explicit solver with automatic time stepping based on the element-by-element stable time increment. The FEM model configuration is shown in Figure 11.

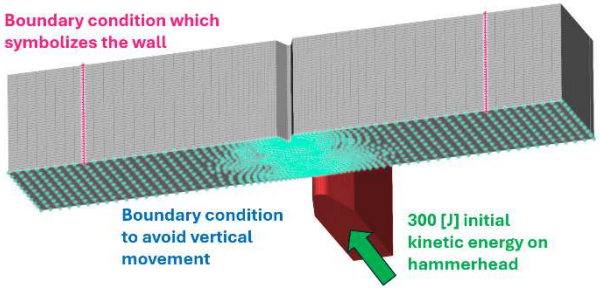


**Figure 11. FEM model of Charpy impact simulation**

The previously calibrated JC constitutive parame–ters, together with the stress triaxiality-dependent da–mage parameters ($D_1$–$D_3$), were assigned to the Charpy impact specimen in the numerical model. The strain rate sensitivity parameter $D_4$ was determined through an iterative calibration procedure, in which its value was

adjusted until the numerically predicted absorbed impact energy matched the experimentally measured Charpy energy.

After several iterations, the optimal agreement between numerical predictions and experimental results was achieved for $D_4 = 0.04375$. With this parameter value, the simulated absorbed impact energy was 119.7 J, which was in close agreement with the experimentally measured value of 119 J.

A comparative analysis of the experimental Charpy impact test and its numerical counterpart indicates that the simulated response reproduces the essential features of the physical test, including crack initiation, propagation, and overall fracture morphology, as illustrated in Figures 12 and 13.

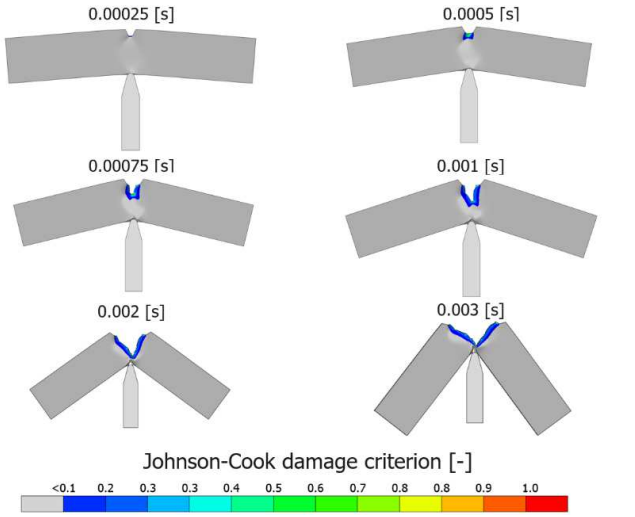


**Figure 12. Simulated fracture progress**

**Figure 13. Experimental specimen and fracture**

## 4. CONCLUSION

In this study, the mechanical behaviour and impact fracture response of L-PBF-fabricated 1.2709 maraging steel were investigated through a combined experimental and numerical approach, with particular emphasis placed on the determination and validation of Johnson–Cook constitutive and damage parameters. Based on the presented results, the following conclusions can be drawn:

Quasi-static uniaxial tensile tests on smooth specimens enabled the reliable identification of the Johnson–Cook constitutive parameters $A$, $B$, and $n$. The model parameters of the JC constitutive relation, $A = 1180$ MPa, $B = 130$ MPa, and $n = 0.1$, for L-PBF 1.2709 steel were obtained using quasi-static tensile tests.

Tensile tests on notched round-bar specimens with varying notch radii, combined with finite-element simulations, proved a practical methodology for determining the stress triaxiality-dependent damage parameters $D_1$, $D_2$, and $D_3$. The numerical evaluation of stress triaxialityproved essential, as analytical estimates deviated significantly from FEM-predicted values due to geometric evolution and stress redistribution during deformation. The $D_1$, $D_2$, and $D_3$ parameters for L-PBF 1.2709 steel were calculated as 0.0688, 6.566, and -3.057, respectively.

The calibrated Johnson–Cook damage model successfully reproduced the experimentally observed force–displacement responses for both smooth and notched tensile specimens, demonstrating its capability to capture damage initiation under different stress states.

An FEM model of the Charpy impact test was developed to represent moderately high strain-rate loading conditions. By iteratively calibrating the strain-rate-sensitivity damage parameter $D_4$, excellent agreement was achieved between the simulated and experimentally measured absorbed impact energies.

Additionally, a linear correlation was observed between stress triaxiality and the area of the cracking fracture surface, further highlighting the influence of stress state on ductile fracture mechanisms in the material.


## ACKNOWLEDGMENT

Project no. 2022-2.1.1-NL-2022-00012 has been implemented with support provided by the Ministry of Culture and Innovation of Hungary from the National Research, Development, and Innovation Fund, financed under the National Laboratories funding scheme.


## REFERENCES


[1] Vashist, V., Istvan, O., Szakal, Z.: Parametric Optimization, Slurry Erosion, and Characterization of 3D Printed Metallic Specimens of Steel 1.2709 and 1.4542, Journal of Materials Engineering and Performance, Vol. 34, pp. 28695-28706, 2025.

[2] Bodziak, S., Al-Rubaie, K.S., Lafratta, F.H., Krmasha, M.N., Rabelo, A., Bohórquez, C.E.N., Chen, Y.: Precipitation in laser powder bed-fused 300-grade maraging steel: Aging at 440 °C for 10 h, Materials Characterization, Vol. 228, 2025.

[3] Strutz, J., Samardžić, I., Šimunović, K.: Optimization potentials of laser powder bed fusion: A conceptual approach, FME Transactions, Vol. 51, No. 3, pp. 432–448, 2023.

[4] Szabó, V., Weltsch, Z.: Full-surface geometric analysis of DMLS-manufactured stainless steel parts after post-processing treatments, Results in Engineering, Vol. 27, 2025.

[5] Erőss, L.D., Markovits, T.: Mass reduction method for topology optimisation of a Ti6Al4V part for additive manufacturing, Production Engineering Archives, Vol. 30, No. 3, pp. 354–360, 2024.

[6] Dehgahi, S., Pirgazi, H., Sanjari, M., Seraj, P., Odeshi, A., Kestens, L.A.I., Mohammadi, M.: Effect of building direction on high strain-rate compressive behavior of heat-treated LPBF-maraging steels using Split Hopkinson pressure bar

apparatus, Materials Science and Engineering: A, Vol. 835, 2022.

[7] Kolomy, S., Jopek, M., Sedlak, J., Benc, M., Zouhar, J.: Study of dynamic behaviour via Taylor anvil test and structure observation of M300 maraging steel fabricated by the selective laser melting method, Journal of Manufacturing Processes, Vol. 125, pp. 283–294, 2024.

[8] Liang, Z., Zhang, Q., Li, W., Li, W., Liang, Z., Zhang, Q., Li, W., Li, W.: Research on the Mechanical Response and Constitutive Model of 18Ni300 Manufactured by SLM with Different Build Directions, Materials, Vol. 17, 2024.

[9] Eisseler, R., Gutsche, D., Maucher, C., Möhring, H.-C.: Inverse Determination of Johnson–Cook Parameters of Additively Produced Anisotropic Maraging Steel, Materials, Vol. 15, No. 1, 2022.

[10] Edwards-Mowforth, M., Costas, M., Kristoffersen, M., Teixeira-Dias, F., Børvik, T.: On the ballistic perforation resistance of additively manufactured and wrought maraging steel: Experiments and numerical models, International Journal of Impact Engineering, Vol. 201, 2025.

[11] Sagar, S., Zhang, Y., Wu, L., Park, H.-Y., Lee, J.-H., Jung, Y.-G., Zhang, J.: Room-Temperature Charpy Impact Property of 3D-Printed 15-5 Stainless Steel, Journal of Materials Engineering and Performance, Vol. 27, No. 1, pp. 52–56, 2018.

[12] Hatos, I., Hargitai, H., Fekete, G., Fekete, I., Hatos, I., Hargitai, H., Fekete, G., Fekete, I.: Effect of Energy Density on the Mechanical Properties of 1.2709 Maraging Steel Produced by Laser Powder Bed Fusion, Materials, Vol. 17, No. 14, 2024.

[13] Aktürk, M., Boy, M., Gupta, M.K., Waqar, S., Krolczyk, G.M., Korkmaz, M.E.: Numerical and experimental investigations of built orientation dependent Johnson–Cook model for selective laser melting manufactured AlSi10Mg, Journal of Materials Research and Technology, Vol. 15, pp. 6244–6259, 2021.

[14] Cao, Y., Zhen, Y., Song, M., Yi, H., Li, F., Li, X.: Determination of Johnson–Cook parameters and evaluation of Charpy impact test performance for X80 pipeline steel, International Journal of Mechanical Sciences, Vol. 179, 2020.

[15] Kumar Reddy Sirigiri, V., Yadav Gudiga, V., Shankar Gattu, U., Suneesh, G., Mohan Buddaraju, K.: A review on Johnson Cook material model, Materials Today: Proceedings, Vol. 62, pp. 3450–3456, 2022.

[16] Khare, S., Kumar, K., Choudhary, S., Singh, P.K., Verma, R.K., Mahajan, P.: Determination of Johnson–Cook Material Parameters for Armour Plate Using DIC and FEM, Metals and Materials International, Vol. 27, No. 12, pp. 4984–4995, 2021.

[17] Banerjee, A., Dhar, S., Acharyya, S., Datta, D., Nayak, N.: Determination of Johnson Cook material and failure model constants and numerical modelling of Charpy impact test of armour steel, Materials Science and Engineering: A, Vol. 640, pp. 200–209, 2015.

[18] Shahanur Hasan, M., De Pellegrin, D., Clegg, R., Yan, C.: Johnson-Cook model parameters determination for 11% and 14% Mn-Steel, Materials Science and Engineering: B, Vol. 283, 2022.

[19] Chtioui, A., Ouballouch, A., Mouchtachi, A.: Investigation of cutting responses during high-speed machining of Ti6Al4V alloy: Finite element analysis, FME Transactions, Vol. 52, No. 4, pp. 616–627, 2024.

[20] Stopel, M., Skibicki, D., Bydgoszcz, A.C.: Determination of the Johnson-Cook damage parameter D4 by Charpy impact testing, Materials Testing, Vol. 60, No. 10, pp. 974–978, 2018.

[21] Standard Test Methods for Notched Bar Impact Testing of Metallic Materials.

## NOMENCLATURE

| | |
|---|---|
| AM | Additive manufacturing |
| L-PBF | Laser powder bed fusion |
| FEM | Finite element method |
| JC | Johnson-Cook |
| CNC | computer numeric control |
| CAX3 | three-node axisymmetric element |
| CAX4 | four-node axisymmetric element |
| A | initial yield strength |
| B | strain hardening modulus |
| n | strain hardening exponent |
| C | strain rate hardening parameter |
| T | temperature |
| $T_{room}$ | environmental temperature |
| $T_{melting}$ | melting temperature |
| $D_1$ | damage parameter 1 |
| $D_2$ | damage parameter 2 |
| $D_3$ | damage parameter 3 |
| $D_4$ | damage parameter 4 |
| $\eta$ | stress triaxiality |
| $\sigma$ | mechanical stress |
| $\varepsilon$ | mechanical strain |
| $\dot{\varepsilon}$ | strain rate |
| $\varepsilon_f$ | fracture strain |

## ОДРЕЂИВАЊЕ ЏОНСОН-КУКОВИХ ПАРАМЕТАРА И ПРОЦЕНА ПЕРФОРМАНСИ ШАРПИЈЕВОГ ТЕСТА УДАРА ЗА ЧЕЛИК 1.2709 ПРОИЗВЕДЕН ПОМОЋУ L-PBF

**Б. Леринц, И. Хатош**

Ласерско фузионисање у слоју праха (L-PBF) омогућава стварање напредних металних делова које је тешко конвенционално произвести. У овој студији одређени су параметри модела Џонсон-Кукове (JC) конститутивне релације и параметри оштећења JC модела отказа за челик 1.2709 произведен помоћу L-PBF. Конститутивни параметри су идентификовани из квазистатичких једноосних тестова затезања спроведених на глатким узорцима. Насупрот томе, параметри оштећења зависни од напона и

триаксијалности одређени су коришћењем тестова затезања на узорцима округлог шипка са зарезом у комбинацији са FEM симулацијама. Криве оптерећења и померања показале су добро слагање са експериментално добијеним подацима. Параметар модела отказа зависан од брзине деформације одређен је корелацијом резултата Шарпијевог теста удара са нумеричким симулацијама. Постигнуто је разумно слагање између симулације и експерименталних резултата. Резултати показују да предложени експериментално-нумерички оквир пружа поуздану основу за моделирање и квазистатичког и ударног понашања челика 1.2709 произведеног помоћу L-PBF.